Spectral analysis of the quiescent low-mass X-ray binary in the globular cluster M30

C.S. Echiburú, S. Guillot, Y. Zhao, C.O. Heinke, F. Ozel, N.A. Webb

Monthly Notices
of the
ROYAL ASTRONOMICAL SOCIETY

MNRAS **495,** 4508–4517 (2020)
Advance Access publication 2020 May 26

doi:10.1093/mnras/staa1456

Spectral analysis of the quiescent low-mass X-ray binary in the globular cluster M30

C. S. Echiburú,[1,2★] S. Guillot,[3★] Y. Zhao,[4] C. O. Heinke,[4] F. Özel[5] and N. A. Webb[3]

[1]*Department of Physics, McGill Space Institute, McGill University, Montreal, QC H3A 2A7, Canada*
[2]*Instituto de Astrofísica, Pontificia Universidad Católica de Chile, Av. Vicuña Mackenna 4860, 7820436 Macul, Santiago, Chile*
[3]*IRAP, Université de Toulouse, CNRS, CNES, F-31028 Toulouse, France*
[4]*Department of Physics, University of Alberta, CCIS 4-183, Edmonton, AB T6G 2E1, Canada*
[5]*Department of Astronomy, University of Arizona, 933 N. Cherry Ave., Tucson, AZ 85721, USA*

Accepted 2020 May 21. Received 2020 May 1; in original form 2020 January 8

ABSTRACT

We present a recent *Chandra* observation of the quiescent low-mass X-ray binary containing a neutron star (NS), located in the globular cluster M30. We fit the thermal emission from the NS to extract its mass and radius. We find no evidence of flux variability between the two observations taken in 2001 and 2017, nor between individual 2017 observations, so we analyse them together to increase the signal-to-noise ratio. We perform simultaneous spectral fits using standard light-element composition atmosphere models (hydrogen or helium), including absorption by the interstellar medium, correction for pile-up of X-ray photons on the detector, and a power law for count excesses at high photon energy. Using a Markov chain Monte Carlo approach, we extract mass and radius credible intervals for both chemical compositions of the atmosphere: $R_{\rm NS} = 7.94^{+0.76}_{-1.21}$ km and $M_{\rm NS} < 1.19$ M$_\odot$ assuming pure hydrogen, and $R_{\rm NS} = 10.50^{+2.88}_{-2.03}$ km and $M_{\rm NS} < 1.78$ M$_\odot$ for helium, where the uncertainties represent the 90 per cent credible regions. For H, the small radius is difficult to reconcile with most current nuclear physics models (especially for nucleonic equations of state) and with other measurements of NS radii, with recent preferred values generally in the 11–14 km range. Whereas for He, the measured radius is consistent with this range. We discuss possible sources of systematic uncertainty that may result in an underestimation of the radius, identifying the presence of surface temperature inhomogeneities as the most relevant bias. According to this, we conclude that either the atmosphere is composed of He or it is anH atmosphere with a significant contribution of hotspots to the observed radiation.

Key words: stars: neutron – globular clusters: individual: M30 – X-rays: binaries.

1 INTRODUCTION

In the complex interior of neutron stars (NSs), and particularly in their cores, matter can be found at extreme densities, higher than 2.8×10^{14} g cm^{-3}, the nuclear matter density. Since those conditions cannot be reproduced on Earth, NSs provide a unique laboratory to study the behaviour of matter at such high densities. The composition and particle interactions are described by an equation of state (EoS), a relation between pressure and energy density at any point inside the star. For a given EoS, solving the Tolman–Oppenheimer–Volkoff equations of stellar structure (Oppenheimer & Volkoff 1939; Tolman 1939) for a range of central densities results in a unique mass–radius ($M_{\rm NS}$-$R_{\rm NS}$) relation for NSs. Therefore, determining $M_{\rm NS}$ or $R_{\rm NS}$ by observational methods (see Özel & Freire 2016, for a recent review) is crucial to discriminate between EoSs proposed by nuclear theory. These are tested by their capability to reproduce the observed macroscopic properties of NSs. Unfortunately, a simultaneous measurement of $M_{\rm NS}$ and $R_{\rm NS}$ is difficult to achieve.

The recently launched Neutron star Interior Composition Explorer (*NICER*; Gendreau & Arzoumanian 2017), a soft X-ray telescope onboard the International Space Station, was designed to address this problem. *NICER* is characterizing the pulse profiles of rotation-powered millisecond pulsars, with a goal of measuring their masses and radii to an accuracy of 5–10 per cent (see Watts 2019, and Miller et al. 2019;Riley et al. 2019 for the measurements of the pulsar PSR J0030+0451). Other mass measurements have been obtained by means of X-ray and optical observations of

★ E-mail: constanza.echiburu@mail.mcgill.ca (CSE); sebastien.guillot@irap.omp.eu (SG)

NSs with high- and low-mass companions (e.g. Rawls et al. 2011), but the most precise masses have generally been extracted from radio timing observations of pulsars in binary systems (e.g. Antoniadis et al. 2012). Radius measurements, on the other hand, are more difficult to achieve, since existing methods suffer from significant systematic errors (see e.g. Miller 2013; Heinke et al. 2014; Bogdanov et al. 2016).

One promising method to constrain NS radii consists of the study of low-mass X-ray binaries (LMXBs) hosting NSs, during quiescence (qLMXBs). Accretion on to compact objects has been observed to be a transient process. When accretion activity increases, X-ray luminosities may rise to $\sim 10^{36-38}$ erg s^{-1} for weeks to months periods. In these outburst episodes, accreted matter accumulates on the NS surface and then form layers of increasing element mass (as a function of depth) due to the large surface gravity. Because of the continuous accretion during outbursts, these accreted layers sink deeper inside the NS crust under the weight of the newer ones, i.e. to high densities, which induces nuclear reactions. The released energy is deposited in the crust and core, heating them up, as explained by *deep crustal heating* (Brown, Bildsten & Rutledge 1998).

In contrast, the quiescent emission observed after active periods of accretion,[1] has typical luminosities in the 10^{32-33} erg s^{-1} range, and can last for periods of years to decades. The origin of this thermal emission is the heat released from the crust and reprocessed by the atmosphere, which then emerges as an $\sim 10^6$ K thermal X-ray spectrum at the surface of the NS.

Since NSs in qLMXBs have been accreting from low-mass stars, and because sedimentation occurs on short time-scales (Alcock & Illarionov 1980; Bildsten, Salpeter & Wasserman 1992), their atmosphere is likely to be composed of hydrogen (Brown, Bildsten & Chang 2002), although this depends on the nature of the donor star which could be H-depleted. On the surface of NSs in qLMXBs, hydrogen is fully ionized due to the high temperatures of $\sim 10^6$ K (Zavlin, Pavlov & Shibanov 1996), facilitating free–free absorption. In these processes, the opacity is given by $\kappa \propto E^{-3}$, where E is the energy of the photon, which causes the atmosphere to be less opaque to photons with larger energies. As a result, photons coming from deeper and hotter layers propagate more easily through the atmosphere, shifting the peak of the spectrum to higher energies (by a factor 1.6–1.8) compared to a blackbody spectrum with the same effective temperature (Rajagopal & Romani 1996; Zavlin et al. 1996).

An atmosphere model allows us to extract the radius measured at infinity $R_\infty = R_{\rm NS}(1+z) = R_{\rm NS}/\sqrt{1-2GM_{\rm NS}/R_{\rm NS}c^2}$ through spectral fitting, but this requires high-quality spectra and, more importantly, knowing the distance to the source. It is known that globular clusters (GCs) host numerous binary systems, due to their high stellar densities and the resulting stellar interactions (Verbunt & Lewin 2006). If the qLMXB is located in a GC with a well-constrained distance,[2] this provides an independent measurement and reduces the uncertainties in the spectral modelling. Another advantage of qLMXBs is that, since they are thought to be the progenitors of millisecond pulsars (e.g. Alpar et al. 1982; Srinivasan & van den Heuvel 1982; Bhattacharya & van den Heuvel 1991; Tauris & van den Heuvel 2006), they are expected to have low magnetic fields, $\ll 10^{10}$ G, such that the opacities remain unaffected by the magnetic field, and so does the emergent spectrum (Zavlin et al. 1996).

Several qLMXBs have been identified in GCs and in the Galactic field (for some examples, see table 4 in Guillot et al. 2009 and references therein). While LMXBs in the field were detected following the onset of a bright accretion outburst, most qLMXBs in GCs, including all those with the highest flux at Earth, have not shown accretion activity.[3] Most of these sources have only been spectrally identified based on their similarities to field LMXBs, observed during quiescence (e.g. Cen X-4 or Aql X-1). Previous works have confirmed that H-atmosphere models accurately describe the spectra of qLMXBs, with radii in the range 10–15 km, as expected for NSs, either from single sources (e.g. Heinke et al. 2006a; Webb & Barret 2007; Guillot, Rutledge & Brown 2011; Heinke et al. 2014; Bogdanov et al. 2016), or from statistical analyses of multiple qLMXBs (e.g. Guillot et al. 2013; Guillot & Rutledge 2014; Lattimer & Steiner 2014; Guillot 2016; Steiner et al. 2018). However, in some cases the accreted material may not be hydrogen, but helium (e.g. Servillat et al. 2012; Catuneanu et al. 2013; Heinke et al. 2014). One way to circumvent this is to identify the nature of the donor star, i.e. to determine the nature of the material transferred on to the NS (e.g. with the detection of an Hα emission line, presumably originating in a faint accretion disc, Haggard et al. 2004). The possibility of helium (or heavier element) atmospheres is well-founded on the existence of ultracompact X-ray binaries (UCXB), with white dwarfs or helium-dominated donors[4] (e.g. Zurek et al. 2009; Altamirano et al. 2010; Sanna et al. 2017; Cadelano et al. 2019). In fact, around 1/3 of the LMXBs in GCs with constraints on the companion nature, possess a white dwarf donor (Bahramian et al. 2014). Since NS He-atmosphere models have harder spectra than H-atmosphere models, using the incorrect composition for the observed thermal emission can result in biases of the inferred radii (Servillat et al. 2012; Heinke et al. 2014).

The motivation for this work is to provide updated $M_{\rm NS}$ and $R_{\rm NS}$ measurements of the NS in the qLMXB located in the core of the GC M30. This source (CXOGLB J214022.13−231045.5, also named M30 A1) was originally reported by Lugger et al. (2007) using a *Chandra* observation obtained in 2001. In that work, the authors considered an H-atmosphere model corrected for pile-up (see description in Section 3). The results were rather unconstrained, with ranges: $7.0 \leq R_{\rm NS} \leq 19.2$ km and $M_{\rm NS} \leq 2.8\,{\rm M}_\odot$. Here, we present new results that include recent deep *Chandra* observations from 2017, using both hydrogen and helium atmospheres. We suggest here a preference for a helium atmosphere composition, which results in an NS radius more compatible with the expected range (from observations of other NSs and from predictions of nuclear theory). However, if the atmosphere is composed of H, the presence of unmodelled hotspots on the surface of the NS could also explain our results.

The paper is organized as follows. In Section 2, we describe the observations and data reduction. In Section 3, we present our analyses prior to the spectral fitting, and our spectral fits. We discuss the results in Section 4. Finally, we present our conclusions in Section 5.

[1] In quiescence, accretion ceases or continues at a very low level $\lesssim 10^{-12}$ M$_\odot$ yr^{-1}.

[2] Typical GC distance measurements have ∼5–10 per cent uncertainties (e.g. O'Malley, Gilligan & Chaboyer 2017).

[3] A few transients hosted in GCs were known to be very faint X-ray sources prior to their first observed outburst, but their quiescent spectrum was too faint to be well characterized (e.g. IGR J17480–2446 in Terzan 5, Heinke et al. 2006b; Bordas et al. 2010; Pooley et al. 2010).

[4] However, only 10^{-20} M$_\odot$ of hydrogen is necessary to produce an optically thick NS atmosphere (Bogdanov et al. 2016), and the matter transferred from He rich donors may still possess enough H to dominate the NS atmosphere, after gravitational settling.

Table 1. Summary of the available *Chandra* observations of M30.

Obs. ID	Starting time	Exposure time (ks)	Count rate[a] (s^{-1})	Detector[b]	Mode
2679	2001-11-19 02:55:12	49.43	0.02	ACIS-S FF	FAINT
18997	2017-09-06 00:05:19	90.19	0.007	ACIS-S 1/8	VFAINT
20725	2017-09-04 16:33:05	17.49	0.007	ACIS-S 1/8	VFAINT
20726	2017-09-10 02:09:13	19.21	0.007	ACIS-S 1/8	VFAINT
20731	2017-09-16 18:04:17	23.99	0.009	ACIS-S 1/8	VFAINT
20732	2017-09-14 14:23:17	47.90	0.007	ACIS-S 1/8	VFAINT
20792	2017-09-18 04:21:43	36.86	0.007	ACIS-S 1/8	VFAINT
20795	2017-09-22 11:39:56	14.33	0.006	ACIS-S 1/8	VFAINT
20796	2017-09-23 06:09:30	30.68	0.007	ACIS-S 1/8	VFAINT

[a]The count rate difference is due to the decrease in the sensitivity of *Chandra*-ACIS at low energies, in the 16 yr that separate the observations (http://cxc.harvard.edu/ciao/why/acisqecontam_previous.html).
[b]'FF' refers to full-frame mode and '1/8' refers to the 1/8 subarray mode.

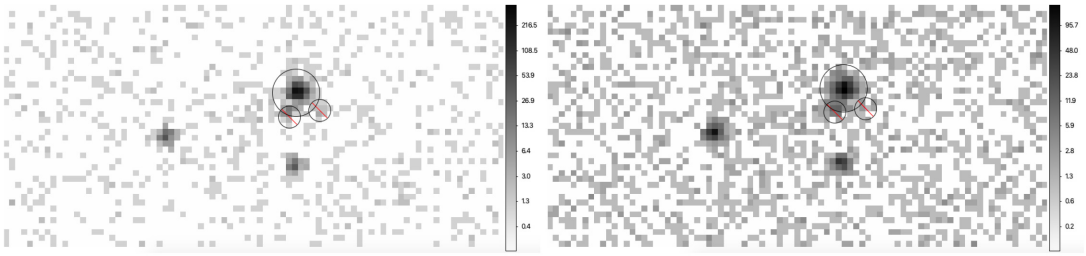

Figure 1. 42 arcsec × 20 arcsec Chandra X-ray images of the qLMXB in M30, in the 0.3–10 keV energy band. The figure shows the extraction regions for two of the observations: ObsID 2679 from 2001 (left) and ObsID 18997 from 2017 (right). The larger circle corresponds to the source region. The two objects located south of the qLMXB (likely to be cataclysmic variables, sources *A*2 and *A*3 in Lugger et al. 2007), are excluded from the source region.

2 OBSERVATIONS AND DATA REDUCTION

In this work, we analyse nine *Chandra* observations of the GC M30, separated in two sets. The first one corresponds to a 49 ks full-frame ACIS-S observation obtained in 2001 and reported in Lugger et al. (2007). In 2017, we obtained eight additional observations with the ACIS-S detector in 1/8 sub-array mode, totalling 281 ks of additional exposure designed to limit the effects of pile-up. Details for both sets of observations are given in Table 1. We performed the data reduction and analysis using CIAO v4.10 (Fruscione et al. 2006), according to the steps suggested in the data preparation thread.[5]The level-1 data were first reprocessed with the latest calibration data base CALDB v4.8.2, running the script `chandra_repro`, which results in new level-2 event files used in the subsequent analysis.

The position of the qLMXB was first reported by Lugger et al. (2007), after astrometric correction with *Hubble Space Telescope* images: $\alpha = 21^{\rm h}40^{\rm m}22\overset{\rm s}{.}130(1)$ and $\delta = -23^{\circ}10'45\overset{''}{.}57(1)$. We extract the source spectra from circular regions of radius 2 arcsec, which ensures that ≈97 per cent of the enclosed energy fraction at 1 keV is included.[6] We used `wavdetect` to obtain the centroid position of the source on each observation, and the extraction is performed following the Step-by-Step guide in the data preparation guide, excluding the two objects south of the qLMXB (see Fig. 1), considering a circular region of radius 0.9 arcsec. These correspond to the sources *A*2 and *A*3 in Lugger et al. (2007).[7] We estimated the number of counts from these two sources possibly contaminating the qLMXB region. For ObsID 2679, we found that 2.2 counts fall within this region, i.e. <0.2 per cent of the total count rate of the qLMXB (∼1100 counts). The background spectra were extracted from a source-free 46.3 arcsec radius circular region near the qLMXB, on the same detector. Notice that the auxiliary response files (ARFs) were corrected for the extraction region. We binned events in each spectrum using the HEASOFT tool `grppha` to 20 counts per bin, in the energy range 0.3–10 keV. Channels below 0.3 keV were ignored because *Chandra*'s calibration is uncertain there, and above 10 keV since the sensitivity of the ACIS instrument decreases rapidly in that range. The instrumental calibration uncertainties were accounted for by adding 3 per cent systematic error. The eight resulting 2017 spectra are combined into a single spectrum using the CIAO tool `combine_spectra`, and then binned following the procedure described before. Therefore, we analyse two spectra: one corresponding to the 2001 observation, and the other corresponding to the combined eight spectra of 2017 observations.

3 SPECTRAL ANALYSIS

The spectral analysis is divided in three parts. First, since the two data sets were obtained 16 yr apart, we search for possible variability of the flux. The second and third parts consist in the simultaneous spectral fits using H and He atmosphere models, respectively. All the spectral fits in this work are performed with the X-ray analysis package XSPEC v12.10.0c (Arnaud 1996) and using χ^2 statistics. We set the 2001 data set as the spectral `group 1` and the 2017 data as the spectral `group 2`. In the following paragraphs, we provide a brief description of each model used for the spectral fits.

[5]http://cxc.harvard.edu/ciao/threads/data.html
[6]*Chandra* Observatory Proposer Guide v21.0, Fig. 6.10, 2018 December.
[7]The analyses of other cluster sources will be reported in Zhao et al., in preparation.

For the H-atmosphere composition, we use the common model `nsatmos` (Heinke et al. 2006a), and for the He-composition, we use the `nsx` model (Ho & Heinke 2009). In both cases, the normalization remains fixed to unity, i.e. assuming that the entire NS surface emits uniformly. We employ a distance $d = 8.20$ kpc to M30 (O'Malley et al. 2017), the most recent value for this globular cluster. The absorption by the interstellar medium is accounted for with the `tbabs` model (Wilms, Allen & McCray 2000), with abundances set to `wilm` (Wilms et al. 2000) and cross-sections set to `vern` (Verner et al. 1996).

We also considered the effect of pile-up (Davis 2001). This phenomenon occurs when two or more photons are registered on a single pixel within one readout time frame of the detector. As a consequence, the readout electronics interpret this event as one photon, with total energy equal to the sum of the energy of the incident photons. This causes a distortion in the shape of the spectrum, and since the inferred NS radius depends on the spectral shape, the effect of unmodelled pile-up could lead to biased radius measurements. The pile-up fractions for the qLMXB in M30 observations are low but not negligible: ∼2 per cent for 2001 data (with 0.062 counts per readout frame), and < 1 per cent for 2017 data (0.006 counts per frame). These were obtained from the *Chandra* proposal tool PIMMS.[8] Nevertheless, such small values can substantially impact the results. For instance, Bogdanov et al. (2016) demonstrated that the inferred radius for the qLMXB X7 in 47Tuc may be underestimated by ∼10 per cent when pile-up effects, even with ∼1 per cent fraction, are neglected. Therefore, modelling pile-up even for a small fraction is fundamental to obtain reliable measurements of $M_{\rm NS}$ and $R_{\rm NS}$. The `pileup` model provided in XSPEC is fully described in Davis (2001). The parameters of this model component are set according to each observation and *The Chandra ABC Guide To Pileup*.[9] We set a frame time of 3.14 s for `group 1` (corresponding to the full-frame mode readout time), and 0.941 s for `group 2` (for the 1/8-frame mode data), while the α parameter of both groups is left untied between the two, and free to vary (see Table 2). The remaining parameters of the pile-up model are fixed to their default values.

Additionally, a high-energy excess has been observed in the tail of some LMXBs in quiescence (e.g. Campana et al. 1998; Rutledge et al. 2002; Campana et al. 2004; Degenaar et al. 2011; Bahramian et al. 2014). Its origin is unclear and might be caused by residual accretion. We explore this possibility by adding a power-law spectral component, `pegpwrlw`, to the `nsatmos` or `nsx` model. To limit degeneracies between the thermal and non-thermal components during the spectral fits, we fix the photon index to 1.5, since the typical range observed for qLMXBs X-ray power spectrum is 1–2, as done in previous analyses of qLMXBs (Guillot et al. 2013; Bogdanov et al. 2016). The power-law energy range is set to its default value, i.e. 2–10 keV, and the power-law normalization is left untied between the two groups.

Finally, to determine the best-fitting parameters and their uncertainties, we employ the `chain` command in XSPEC that performs Markov chain Monte Carlo (MCMC) simulations to obtain the posterior distributions of all fitted parameters. The MCMC is initialized from the best fit, with 200 000 steps, 100 walkers, and burn-in corresponding to 25 per cent of the chain length. The priors are uniformly distributed within the hard limits of the `nsatmos` or `nsx` parameters. For `nsatmos`, these are 0.5–3.0 $M_\odot$ for $M_{\rm NS}$, 5–30 km for $R_{\rm NS}$, and 5–6.5 for $\log T_{\rm eff}$/K. The `nsx` model shares the same limits, except for $\log T_{\rm eff}$/K, covering the 5.5–6.7 range. All uncertainties reported hereafter are at the 90 per cent confidence level, or correspond to the 90 per cent credible interval when derived from the MCMC posterior distributions, unless specified otherwise.

Table 2. Spectral fit parameters for `nsatmos` and `nsx`. The statistical fits are χ^2_ν/dof (prob.) = 0.96/105 (0.59) for `nsatmos`, and χ^2_ν/dof (prob.) = 0.98/105 (0.55) for `nsx`. The values in parentheses correspond to fixed parameters in the models, while other values are obtained from the MCMC posterior medians. All reported uncertainties correspond to the 5 per cent and 95 per cent quantiles, i.e. representing the 90 per cent credible intervals.

Model parameter	Group 1 (2001)	Group 2 (2017)
`nsatmos`		
Frame time (s)	(3.14)	(0.941)
$\alpha_{\rm pileup}$	$0.18^{+0.56}_{-0.17}$	$0.53^{+0.43}_{-0.48}$
$N_{\rm H}$ (10^{20} cm^{-2})[a]	< 0.61	
kTeff (eV)	$107.72^{+19.63}_{-6.78}$	
$M_{\rm NS}$ ($M_\odot$)[b]	$0.79^{+0.40}_{-0.28}$	
$R_{\rm NS}$ (km)	$7.94^{+0.76}_{-1.21}$	
Γ[c]	(1.5)	
PL Norm (10^{-15} erg s^{-1} cm^{-2})	< 0.002[a]	$2.30^{+1.47}_{-1.45}$
`nsx`		
Frame time (s)	(3.14)	(0.941)
$\alpha_{\rm pileup}$	$0.02^{+0.60}_{-0.02}$	<0.1[a]
$N_{\rm H}$ (10^{20} cm^{-2})	$1.74^{+2.87}_{-1.40}$	
$kT_{\rm eff}$ (eV)	$96.28^{+21.30}_{-9.90}$	
$M_{\rm NS}$ ($M_\odot$)[b]	$1.07^{+0.71}_{-0.51}$	
$R_{\rm NS}$ (km)	$10.50^{+2.88}_{-2.03}$	
Γ[c]	(1.5)	
PL Norm (10^{-15} erg s^{-1} cm^{-2})	< 0.0004[a]	$2.21^{+1.62}_{-1.44}$

[a]Corresponds to the 90 per cent confidence upper limit.
[b]Note that the lower limit of the parameter is unconstrained, and consistent with the hard limit of the model, imposed by the prior. Since the median value may be also affected, the most meaningful value is the upper limit.
[c]Represents the photon index of the power-law model.

3.1 Flux variability

The X-ray flux of qLMXBs is not expected to show variability during quiescence, unless an accretion episode happened recently.[10] However, such an event would likely be detected by all-sky monitors, as was the case for IGR J17480−2446 in Terzan 5 (Bordas et al. 2010; Pooley et al. 2010). We search for signs of flux variation over the 16 yr between the two observations, and additionally, between the individual 2017 observations. The lack of variability would allow us to fit both spectra simultaneously with tied NS parameters. If the spectra show variability, it would, however, imply a change in temperature or in the normalization of the thermal spectrum. That was observed in two qLMXBs (in NGC 6440 CX 1 and Terzan 5 CX 12, Cackett et al. 2005; Bahramian et al. 2015; Walsh, Cackett & Bernardini 2015), which showed marginal evidence of variations due to low-level accretion.

[8]https://asc.harvard.edu/toolkit/pimms.jsp
[9]http://cxc.harvard.edu/ciao/download/doc/pileup_abc.pdf

[10]Typical returns to quiescence flux levels following an outburst can last several years (e.g. Wijnands, Degenaar & Page 2017, for a short review).

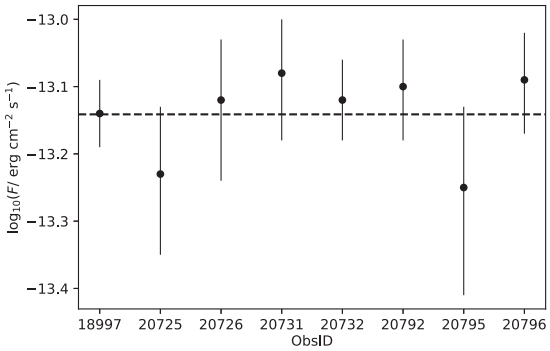

Figure 2. Flux estimation and 2σ error bars for individual 2017 observations. The dashed line indicates the best-fitting flux $\log_{10}(F/\,\mathrm{erg\ cm^{-2}\ s^{-1}}) = -13.14^{+0.02}_{-0.02}$ ($\chi^2_\nu = 0.004$) obtained from least-squares fitting method, where the error corresponds to the estimated standard error for the best-fitting value.

We begin by testing for flux variations in time-scales of years. For this exercise, the spectral model `tbabs*nsatmos` was convolved with `cflux`, a XSPEC model used to estimate the flux of the other components, and their corresponding uncertainties. We fit the data of `group 1` (2001) and `group 2` (2017) with all parameters untied. The spectral fit results in fluxes $\log_{10}(F_{2001}/\,\mathrm{erg\ cm^{-2}\ s^{-1}}) = -13.12^{+0.03}_{-0.03}$ for the 2001 data, and $\log_{10}(F_{2017}/\,\mathrm{erg\ cm^{-2}\ s^{-1}}) = -13.11^{+0.03}_{-0.03}$ for the 2017 data. The temperatures were measured independently using the spectral model `pileup*tbabs*nsatmos` (see Section 3.2). We find $kT_{\rm eff} = 104.23^{+23.48}_{-14.26}$ eV for the 2001 data, and $kT_{\rm eff} = 112.58^{+25.06}_{-10.79}$ eV for the 2017 data. For this spectral fit, we found a statistically acceptable result, with $\chi^2/\mathrm{dof} \equiv \chi^2_\nu = 0.97$, where dof is the number of degrees of freedom, corresponding to 101, and null hypothesis probability (nhp) equal to 0.58. Therefore, there is no evidence of flux variability of this source between 2001 and 2017.

Additionally, we tested an alternative method to search for flux variability. For this exercise we fit the model `pileup*tbabs*(const*nsatmos)`, fixing `const` to 1 in `group 2`, and with the remainder parameters free and tied between the two groups. Here, the `const` factor represents the relative normalization of the two fluxes. We found a value of the constant consistent with unity, $0.97^{+0.11}_{-0.10}$, were the errors correspond to the 99 per cent confidence estimated with `error` command. Thus, there are no signs of flux variability, leading to the same conclusion.

The quiescent spectrum of LMXBs can also show short-term variability over time-scales of days (e.g. Rivera Sandoval et al. 2018). Therefore, we search for flux variations within the individual observations taken in 2017. Due to the low number of counts in most 2017 observations (except ObsIDs 18997 and 20792), we rebin the data following the procedure described in Section 2 but using a minimum of 15 counts per bin. We fit the spectral model `tbabs*nsatmos` convolved with `cflux` to each observation, and computed the best-fitting flux from MCMC runs. We do not include the `pileup` model, since 2017 data were obtained in 1/8-frame mode to reduce pile-up fraction, making this model difficult to constrain given the count rates shown in Table 1. The results are shown in Fig. 2 (see also Table A2), and indicate the flux is constant within uncertainties, placing this source among the few steady qLMXB reliable for measuring radii (e.g. Heinke et al. 2006a; Servillat et al. 2012; Guillot et al. 2013).

3.2 Hydrogen and helium atmospheres

The spectral fitting is performed by assigning the same set of parameters to both data groups, i.e. keeping the NS temperature, mass, and radius tied between the two groups. All the parameters are left free, except for the distance, the H/He normalization, the photon index, and the pile-up parameters mentioned previously. The spectral fit to the model `pileup*tbabs*(nsatmos + pegpwrlw)` results in a statistically acceptable fit with $\chi^2_\nu = 0.96$ with nhp = 0.59 and is shown in Fig. 3. From the MCMC posterior distributions, we deduce the median values as well as the 5 per cent and 95 per cent quantiles, which give us the 90 per cent credible intervals of the parameters. All results are summarized in Table 2, and the one- and two-dimensions posterior distributions are displayed in Fig. 4. In particular, we find $R_{\rm NS} = 7.94^{+0.76}_{-1.21}$ km and $M_{\rm NS} = 0.79^{+0.40}_{-0.28}$ $\mathrm{M}_\odot$. It is important to emphasize that the lower limit in the mass parameter is technically unconstrained, since it is consistent with the hard limit of the model. Because the hard limit defines a range for the prior, it likely affects both the lower limit and the median values. For this reason we note that the less affected and most informative value is the upper limit of this parameter. These results are physically unrealistic for an EoS that can support a 2 $\mathrm{M}_\odot$ NS (e.g. Özel & Freire 2016), but consistent with the previously reported range for this source (7.0 km $\leq R_{\rm NS} \leq$ 19.2 km, at 90 per cent confidence, Lugger et al. 2007). Since assumptions of H-atmospheric composition may lead to an underestimation of the NS radius (see Section 1), we next consider an atmosphere composed of pure helium.

This analysis is performed following the same procedure described before, but with the `nsx` model[11] (Ho & Heinke 2009), i.e. `pileup*tbabs*(nsx + pegpwrlw)`. The results of the statistically acceptable fit ($\chi^2_\nu = 0.98$ with nhp = 0.55) are shown in Table 2 and Figs 3 and 4. Again, we use MCMC simulations to obtain the posterior distributions of the parameters. As expected, we find larger inferred values for $R_{\rm NS}$ and $M_{\rm NS}$: $R_{\rm NS} = 10.50^{+2.88}_{-2.03}$ km and $M_{\rm NS} = 1.07^{+0.71}_{-0.51}$ $\mathrm{M}_\odot$. As explained before, note that the most meaningful value is the upper limit of the mass parameter. These results are easier to reconcile with other measurements of these two NS properties (Özel & Freire 2016), and based on this, one can argue that our data are better described by an He atmosphere model. The best-fitting $N_{\rm H}$ obtained with `nsx` appears consistent with that deduced from the $N_{\rm H}$–$E(B-V)$ relations (Foight et al. 2016, for a recent estimate), predicting $N_{\rm H} \sim 2.8\times10^{20}\,\mathrm{cm^{-2}}$, for $E(B-V) = 0.03$ (Harris 1996, 2010). While this consistency is interesting, it is important to keep in mind that $N_{\rm H}$–$E(B-V)$ relations may be uncertain, especially for low absorption. None the less, it is important to note that H and He models describe equally well the data, and are virtually indistinguishable at the signal-to-noise ratio available from current X-ray observatories.

Additionally, to explore the impact of adding a power law to both models, we repeated the spectral fits without considering this component. The spectral fit to the model `pileup*tbabs*nsatmos` results in $\chi^2_\nu = 0.99$ with nhp = 0.49. The measured properties are $R_{\rm NS} = 6.51^{+1.79}_{-1.40}$ km and $M_{\rm NS} = 1.16^{+0.17}_{-0.45}$ $\mathrm{M}_\odot$. While in the case of `pileup*tbabs*nsx`, the spectral fit results in $\chi^2_\nu = 0.99$ with nhp = 0.51, $R_{\rm NS} = 8.05^{+2.49}_{-1.87}$ km, and $M_{\rm NS} = 1.39^{+0.32}_{-0.58}$ $\mathrm{M}_\odot$. These results are consistent with those of the previous spectral fits, however, they suggest even smaller $R_{\rm NS}$. Together with the

[11] A 'switch' parameter for `nsx` permits selecting He or carbon composition.

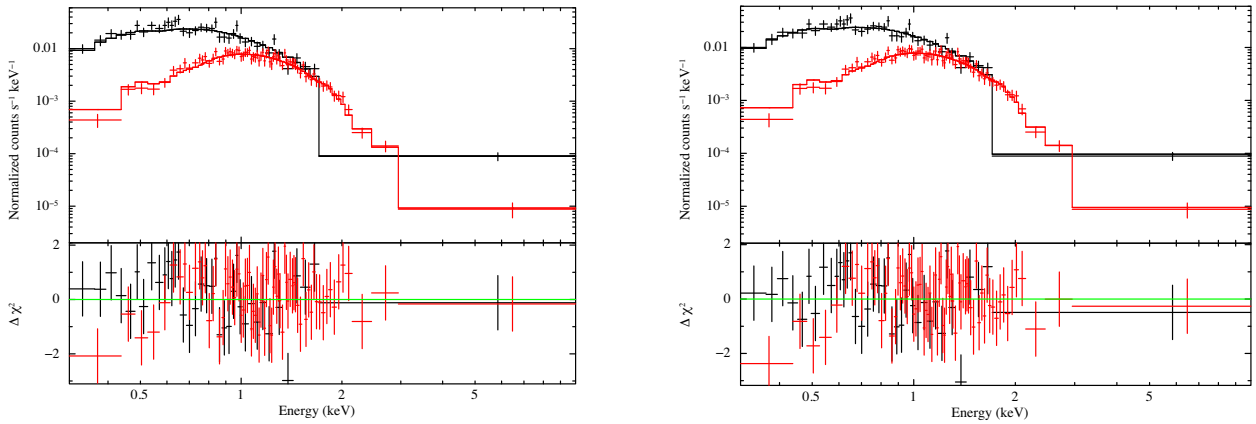

Figure 3. Spectra of the qLMXB in M30 from the 2001 (black) and 2017 (red) observations, where the reduced sensitivity of *Chandra* in those 16 yr can be noticed at low energies. The solid lines represent the best fit to a `nsatmos` H-atmosphere (left) and `nsx` He-atmosphere (right) model. In both cases, a Galactic absorption component (`tbabs`), a power-law component (with photon index fixed to 1.5), and a pile-up correction model are included. The bottom panels display the differences between data points and the best-fitting models.

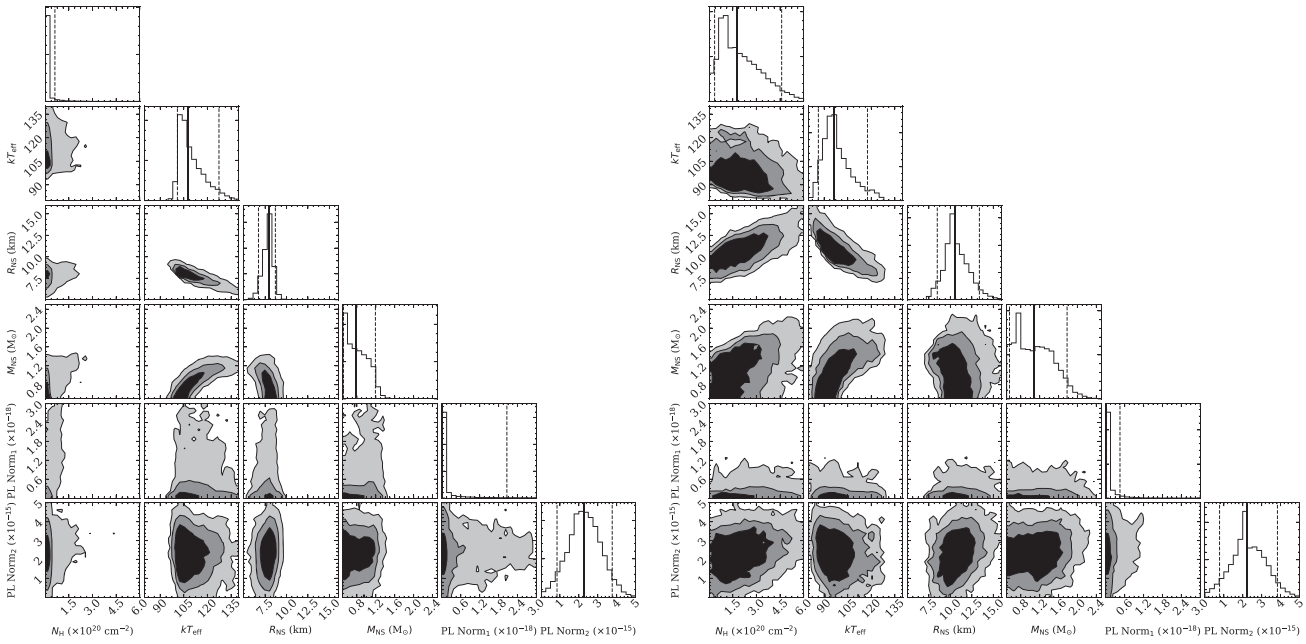

Figure 4. The one- and two-dimensional MCMC posterior distributions for the parameters in the spectral fitting (Section 3.2). The black, dark grey, and light grey regions correspond to the 68 per cent, 90 per cent, and 99 per cent credible intervals, respectively, for the `nsatmos` H-atmosphere (left) and `nsx` He-atmosphere (right) models. The solid line in the one-dimensional posterior distributions represents the median value, while the left/right dashed lines represent the 5 per cent and 95 per cent percentiles, respectively. Note that in the mass parameter the lower limit is technically unconstrained, since it is consistent with the hard limit of `nsatmos` and `nsx` models. In both figures, the power-law normalization of group 1 (PL Norm$_1$) and group 2 (PL Norm$_2$) are measured in units of erg s^{-1} cm^{-2}.

power-law normalizations of 2017 (marginally consistent with zero, see the posterior distributions in Fig. 4), this indicates a possible non-negligible contribution of the power-law component to the seemingly purely thermal spectrum. Moreover, if a non-thermal component is indeed present and not accounted for, it may skew the R_{NS} measurement. Because it is appropriate to include the power-law component when trying to place constraints on the radius, we favour our analyses including the power law.

Using the `simftest` tool in XSPEC, we also determine the significance of adding an extra power-law component (`pegpwrlw`) to the `pileup*tbabs*nsatmos` model. After 1000 iterations with `simftest`, we find a probability of 0.02 that the data are consistent with the simpler model, i.e. without the power-law component. Likewise, employing `simftest` to the model `pileup*tbabs*(nsx + pegpwrlw)` results in a probability of 0.04 that the data are consistent with the model without the `pegpwrlw` component. Both represent marginal evidence that the power-law component is required. Therefore, we add this component to account for the uncertainties it may cause, as explained previously.

We also repeated all the reported analyses without combining the eight 2017 spectra. The results are shown in Table A1. Though

we find consistent results, we note the uncertainties are slightly larger, especially for the radius measurements. In particular, when fitting an H atmosphere the upper limit for $R_{\rm NS}$ seems to be consistent with typical NS radii. However, we favour our analyses with combined 2017 spectra, since the precision of measurements is substantially increased.

Finally, due to the reduced sensitivity of *Chandra* at low energies (see Fig. 3), we tested that the calibration of the degraded response did not affect the results, and found that the measured radius did not change when using a 6-month old response matrix.

4 DISCUSSION

Our spectral analysis of the qLMXB in the GC M30 seems to favour the He atmosphere model, according to the radius obtained, but it reveals a relatively small radius when using an H model, in apparent disagreement with theoretical and previous experimental studies (see Lattimer & Prakash 2016, for a recent review). Specifically, an NS with radius $R_{\rm NS} = 7.94^{+0.76}_{-1.21}$ km is impossible to reconcile with nucleonic EoS models, especially when those are constrained by NS mass measurements around $\sim 2\,{\rm M}_{\odot}$ (Demorest et al. 2010; Antoniadis et al. 2013; Cromartie et al. 2019). Such measurements impose a certain stiffness to the EoS which then corresponds to NSs with $R_{\rm NS} \gtrsim 11$ km. Strange quark stars models could, however, be compatible with the radius measurement obtained with the H atmosphere model (Haensel, Zdunik & Schaefer 1986; Lattimer & Prakash 2001). We none the less insist that this is insufficient evidence to claim that this qLMXB in M30 hosts a quark star. The NS radius inferred from qLMXB observations is highly sensitive to the spectral shape, and it is fundamental to explore possible biases induced by the assumptions made in the present analysis. Motivated by this, we discuss below the most relevant and dominant sources of systematic uncertainty.

4.1 Chemical composition of the atmosphere

The assumption on the atmospheric composition directly impacts the resulting $M_{\rm NS}$ and $R_{\rm NS}$ measurements and several studies have shown that the R_{∞} measured could be underestimated by 20–50 per cent if an H-atmosphere model is assumed, when an He-atmosphere is actually present atop the NS (Servillat et al. 2012; Catuneanu et al. 2013; Heinke et al. 2014; Bogdanov et al. 2016; Steiner et al. 2018). In these works and in this one, both H and He atmosphere models fit the data equally well. Spectral analyses alone cannot distinguish between the two possible compositions.

As stated before, while the atmospheric composition of an NS in a qLMXB is expected to be pure H, it depends on the nature of the donor star. In UCXBs, the companion star could be a helium star or a white dwarf. In fact, some of them are known to possess a helium-rich donor star (Altamirano et al. 2010; Sanna et al. 2017; Cadelano et al. 2019), or to exhibit He-ignition bursts from the NS surface indicating accretion of He (see Strohmayer & Bildsten 2006, for a review).

Identifying the presence of hydrogen in an LMXB system, or understanding the nature of the donor is key to determine the atmosphere composition of the NS. This can be achieved by the detection of an Hα emission line in its optical spectrum, which would indicate the presence of a hydrogen-rich accretion disc (see Haggard et al. 2004, for the qLMXB in ω Cen). If H is transferred on to the NS, then the surface (i.e. the atmosphere) must necessarily be composed of hydrogen. Alternatively, evidence of H composition may be proved by measuring the orbital period of the binary. As in the case of the qLMXB X5 in 47 Tuc, the 8.666 ± 0.008 h eclipse period allowed to constrain the properties of the companion, indicating it must be a main-sequence (MS) star (Heinke et al. 2002).

For the qLMXB in M30, the orbital period is unknown, no information is available on the nature of the companion star or on the presence of H in the binary system. These imply that the chemical composition of the NS atmosphere remains uncertain, and an He composition cannot be excluded.

Even if the donor star is H-rich, another process that may alter the chemical composition of an NS atmosphere is the nuclear diffuse burning of H into He, where an underlying layer can consume H by capturing protons on time-scales of 10^4–10^5 yr (Chang & Bildsten 2003, 2004). The H depletion implies a heavier element composition of the external atmosphere (e.g. Chang, Bildsten & Arras 2010), favouring an He composition. If that is the case, and given the large time-scale of the process, another source of heating is required to account for the $\sim 10^{33}$ erg s^{-1} luminosity. An example of this are the new class of NSs known as 'hot widows', thought to be descendants of NSs in LMXBs, which are powered by r-mode instability, capable of maintaining high temperatures during $\sim 10^9$ yr (Chugunov, Gusakov & Kantor 2014). The nuclear diffusive burning scenario requires that no continuing accretion is occurring, as it would quickly replenish the atmosphere with H. However, the presence of the variable power-law component strongly suggests there is continuing accretion. Otherwise, it could represent a propeller shock, meaning that the material does not land on the NS surface, and allowing the nuclear diffusive burning hypothesis.

4.2 Surface temperature inhomogeneities

To model the emission from the NS, we assumed that the entire surface emits uniformly. However, unmodelled surface inhomogeneities, e.g. surface hotspots, could bias the measured radius. The presence of hotspots on the surface of the NS could be detectable as pulsed emission depending on the circumstances, e.g. the size, temperature, and location of the spots, or the inclination of the observer with respect to the rotation axis (Elshamouty et al. 2016). To detect such pulsations an instrument with high timing resolution and high sensitivity is required. Currently, there are no X-ray observations of qLMXBs with sufficient timing resolution, except for deep *Chandra* High Resolution Camera observations of 47 Tuc (Cameron et al. 2007), and M28 (Rutledge et al. 2004).

Ignoring a possible surface hotspot when modelling the emission spectrum would result in a measured temperature higher than the true value, and therefore a radius smaller than the actual NS value. Elshamouty et al. (2016) carefully studied the biases caused by unmodelled hotspots on the surface of NSs in qLMXBs; basing their calculations on the upper limit on the pulsed fraction for the qLMXB X7 in 47 Tuc, $\lesssim 16$ per cent, obtained from the *Chandra*-HRC observations. They determined that, in the case of 47 Tuc X7, not modelling hotspots that might be present on the NS surface would cause an underestimation of the radius by as much as ~ 25 per cent (Elshamouty et al. 2016). In this context, we tested the presence of a hotspot by fitting the model `pileup*tbabs*(nsatmos + pegpwrlw)` with `nsatmos` normalization free to vary, a fixed radius $R_{\rm NS} = 12$ km, and power-law photon index $\Gamma = 1.5$. The result of the spectral fit is an emitting area of 38^{+9}_{-6} per cent of the total NS surface, where the uncertainty corresponds to the 90 per cent confidence computed with `error`

command. Since typically hotspot sizes represent less than 2 per cent of the surface emitting area (e.g. Guillot et al. 2016), we conclude the area given by the fit is probably larger than a hotspot. However, it is consistent with a spectrum that combines the emission from the full surface and a small hotspot.

The present *Chandra*-ACIS observations of M30 lack the time resolution (and the sensitivity) to search for the existence of hotspots. However, they highly motivate searches for X-ray pulsations in the future. The *NICER* (Gendreau & Arzoumanian 2017) could address this issue (Ray, Arzoumanian & Gendreau 2018), but the non-imaging capabilities will somewhat complicate the search for pulsations in the crowded field of GCs. In the next decade, the *Athena X-ray Observatory* (Nandra et al. 2013) will be able to provide X-ray data with high sensitivity, 10 μs time resolution and ∼5 arcsec spatial resolution, that will facilitate the search for the presence of X-ray pulsations as evidence of hotspots at the surface of NSs in qLMXBs.

4.3 Rotational corrections

In this work, we have made the assumption that the NS is spherically symmetric and is not rotating. However, some NSs rotate at high frequencies extending up to 716 Hz (Hessels et al. 2006), and implying surface velocities $\gtrsim 0.1c$, as revealed from their radio pulsations. Other NSs spin frequencies have been discovered due to their X-ray pulsations, as the case of accreting millisecond X-ray pulsars, rotating hundreds of times per second (see Patruno & Watts 2012, for a review).

The effect of fast rotation is to distort the spectrum with respect to a non-rotating one, because photons experience a Doppler shift when they are emitted from the approaching or receding side of the stellar surface. Also, such rapid spins distort the shape of the surface, which becomes oblate (AlGendy & Morsink 2014). Thus, the fast rotation of NSs may impact the observed thermal spectrum, and consequently, bias the measurements of the spectroscopic radius R_∞ by a few per cent. Bauböck et al. (2015) quantified the bias in the inferred R_∞ when the non-spinning case is assumed compared to a spinning case, from moderate to fast rotation.

The corrections to the radius R_∞ depend on the NS spin, but also on its compactness (i.e. on $M_{\rm NS}$ and $R_{\rm NS}$) and on the observer's viewing angle with respect to the rotation axis. Not considering these corrections result in an underestimation of the flux by as much as 12 per cent, the worst case scenario being for an edge-on fast rotating NS (∼600 Hz) with a 15 km radius. Bauböck et al. (2015) estimated the incurred bias on the measured NS radius which can be as much as 10 per cent for a 800 Hz, 15 km NS. For more realistic NS properties (e.g. a 11 km NS spinning at 600 Hz), the radius could be underestimated by ∼ 2.5 per cent if the rotational correction are neglected. Note that these corrections were calculated for the blackbody case, which may be different from the H-atmosphere case (Amason & Morsink, in preparation).

Unfortunately, for the NS in the M30 qLMXB, like for most qLMXBs in GCs, the spin frequency is unknown, since these objects do not exhibit radio emission, and their (likely) uniform surface temperature precludes the detection of pulsations in the X-ray band. However, if surface inhomogeneities are present, future missions will be capable of detecting them, as discussed in Section 4.2.

4.4 Distance

Another source of uncertainty in the radius measurements is the distance d to the GC hosting the qLMXB, since $F \sim (R_\infty/d)^2$. We considered the most recent distance measurement to M30, 8.2 ± 0.62 kpc (1σ, O'Malley et al. 2017), determined with the MS fitting method, which consists in matching the MS stars of the GC to a theoretical MS in a colour–magnitude diagram (CMD). The latter is obtained from stellar models, which require calibrations using stars with known distances. The GC MS is shifted until it matches the theoretical one, and that shift is related to the *distance modulus*, allowing to estimate the distance. The reported value of 8.2 ± 0.62 kpc incorporates uncertainties associated with the theoretical model, the photometric measurements, metallicity and reddening estimates, which could affect the location of the stars in the CMD.

The uncertainty in the source distance adds to the uncertainty on R_∞, and therefore on $R_{\rm NS}$. In the case of M30, the distance uncertainty of ±7.6 per cent (at 1σ confidence) is not dominant compared to the other sources of uncertainties discussed above, such as the chemical composition of the atmosphere, or surface temperature inhomogeneities. Moreover, it is smaller than the statistical uncertainties on the radius in our results. Thus, the uncertainty on d was not included in our analysis. In the near future, precise measurements of the distance to GCs are expected to be achievable with the next *Gaia* data release, permitting distances with uncertainties better than 1 per cent (Pancino et al. 2017).

5 CONCLUSIONS

In this work, we have performed a spectral analysis of two archived *Chandra* observations of the qLMXB, CXOGLB J214022.13−231045.5, in the GC M30. Because the two observations are separated by 16 yr, we first confirmed that the flux remained constant at 90 per cent confidence. We then performed a simultaneous spectral analysis of the two data sets using a model commonly used for qLMXB: a light-element composition atmosphere (H/He), absorbed by interstellar medium, corrected for pile-up, and a power law for count excesses at high energies. Our main conclusions are the following:

(1) The spectral fit performed with the H-atmosphere model `nsatmos` results in relatively small radii, but consistent, compared to the previous results reported by Lugger et al. (2007). The MCMC simulations we performed to quantify the parameters' credible regions give a measured radius $R_{\rm NS} = 7.94^{+0.76}_{-1.21}$ km and a mass $M_{\rm NS} < 1.19$ M$_\odot$.

(2) When considering the He-atmosphere model `nsx`, the measured radius and mass are somewhat larger, as expected, $R_{\rm NS} = 10.50^{+2.88}_{-2.03}$ km and $M_{\rm NS} < 1.78$ M$_\odot$, but consistent with typically measured values for qLMXBs and other classes of NSs (Özel & Freire 2016). However, it is worth to mention that the error range is large enough to include most of both the observed and predicted ranges. Because this spectral model results in NS properties that are less at odds with previous measurements, we tentatively conclude that it provides a more appropriate description of the qLMXB in M30.

(3) We find that a variable power-law component is required in addition to the thermal component (`nsatmos` or `nsx`), to properly constrain the $R_{\rm NS}$ measurement.

Identifying the companion star, or verifying the presence of H or He in the qLMXB system, will determine the spectral model to use for the X-ray spectrum of this source. Other sources of uncertainties and biases discussed in Section 4, in particular those that cause an underestimation of the radius (surface temperature inhomogeneities, being the strongest source of bias, since it accounts for ∼25 per cent of uncertainty) could possibly make the H

radius reported above more compatible with NS radii in the 11–14 km range that have been reported recently (e.g. Nättilä et al. 2017; Abbott et al. 2018; Baillot d'Etivaux et al. 2019; González-Caniulef, Guillot & Reisenegger 2019; Raaijmakers et al. 2019, 2020).

ACKNOWLEDGEMENTS

CSE acknowledges the support of the Fondo Nacional de Desarrollo Científico y Tecnológico (FONDECYT) Regular Project 1150411 during the early stages of this work, the funding from McGill's Wolfe Fellowship in Scientific and Technological Literacy, the McGill Space Institute, and the Canadian Institute for Advanced Research (CIFAR). CSE also thanks Daryl Haggard for valuable discussions. SG and NAW acknowledge the support of the French Centre National d'Études Spatiales (CNES). COH is supported by the Natural Sciences and Engineering Research Council of Canada (NSERC) Discovery Grant RGPIN-2016-04602, and a Discovery Accelerator Supplement. We also acknowledge extensive use of NASA's Astrophysics Data System (ADS) Bibliographic Services and the ArXiv. Finally, we acknowledge the Chandra scheduling, data processing, and archive teams for making these observations possible.

REFERENCES

Abbott B. P. et al., 2018, Phys. Rev. Lett., 121, 161101
Alcock C., Illarionov A., 1980, ApJ, 235, 534
AlGendy M., Morsink S. M., 2014, ApJ, 791, 78
Alpar M. A., Cheng A. F., Ruderman M. A., Shaham J., 1982, Nature, 300, 728
Altamirano D. et al., 2010, ApJ, 712, L58
Antoniadis J., van Kerkwijk M. H., Koester D., Freire P. C. C., Wex N., Tauris T. M., Kramer M., Bassa C. G., 2012, MNRAS, 423, 3316
Antoniadis J. et al., 2013, Science, 340, 448
Arnaud K. A., 1996, in Jacoby G. H., Barnes J., eds, ASP Conf. Ser. Vol. 101, Astronomical Data Analysis Software and Systems V. Astron. Soc. Pac., San Francisco, p. 17
Bahramian A. et al., 2014, ApJ, 780, 127
Bahramian A., Heinke C. O., Degenaar N., Chomiuk L., Wijnands R., Strader J., Ho W. C. G., Pooley D., 2015, MNRAS, 452, 3475
Baillot d'Etivaux N., Guillot S., Margueron J., Webb N., Catelan M., Reisenegger A., 2019, ApJ, 887, 48
Bauböck M., Özel F., Psaltis D., Morsink S. M., 2015, ApJ, 799, 22
Bhattacharya D., van den Heuvel E. P. J., 1991, Phys. Rep., 203, 1
Bildsten L., Salpeter E. E., Wasserman I., 1992, ApJ, 384, 143
Bogdanov S., Heinke C. O., Özel F., Güver T., 2016, ApJ, 831, 184
Bordas P. et al., 2010, Astron. Telegram, 2919, 1
Brown E. F., Bildsten L., Rutledge R. E., 1998, ApJ, 504, L95
Brown E. F., Bildsten L., Chang P., 2002, ApJ, 574, 920
Cackett E. M. et al., 2005, ApJ, 620, 922
Cadelano M., Ferraro F. R., Istrate A. G., Pallanca C., Lanzoni B., Freire P. C. C., 2019, ApJ, 875, 25
Cameron P. B., Rutledge R. E., Camilo F., Bildsten L., Ransom S. M., Kulkarni S. R., 2007, ApJ, 660, 587
Campana S., Colpi M., Mereghetti S., Stella L., Tavani M., 1998, A&AR, 8, 279
Campana S., Israel G. L., Stella L., Gastaldello F., Mereghetti S., 2004, ApJ, 601, 474
Catuneanu A., Heinke C. O., Sivakoff G. R., Ho W. C. G., Servillat M., 2013, ApJ, 764, 145
Chang P., Bildsten L., 2003, ApJ, 585, 464
Chang P., Bildsten L., 2004, ApJ, 605, 830
Chang P., Bildsten L., Arras P., 2010, ApJ, 723, 719
Chugunov A. I., Gusakov M. E., Kantor E. M., 2014, MNRAS, 445, 385
Cromartie H. T. et al., 2019, Nat. Astron., 4, 72
Davis J. E., 2001, ApJ, 562, 575
Degenaar N. et al., 2011, MNRAS, 412, 1409
Demorest P. B., Pennucci T., Ransom S. M., Roberts M. S. E., Hessels J. W. T., 2010, Nature, 467, 1081
Elshamouty K. G., Heinke C. O., Morsink S. M., Bogdanov S., Stevens A. L., 2016, ApJ, 826, 162
Foight D. R., Güver T., Özel F., Slane P. O., 2016, ApJ, 826, 66
Fruscione A. et al., 2006, in Silva D. R., Doxsey R. E., eds, Proc. SPIE Conf. Ser. Vol. 6270, Observatory Operations: Strategies, Processes, and Systems. SPIE, Bellingham, p. 62701V
Gendreau K., Arzoumanian Z., 2017, Nat. Astron., 1, 895
González-Caniulef D., Guillot S., Reisenegger A., 2019, MNRAS, 490, 5848
Guillot S., 2016, Mem. Soc. Astron. Ital., 87, 521
Guillot S., Rutledge R. E., 2014, ApJ, 796, L3
Guillot S., Rutledge R. E., Bildsten L., Brown E. F., Pavlov G. G., Zavlin V. E., 2009, MNRAS, 392, 665
Guillot S., Rutledge R. E., Brown E. F., 2011, ApJ, 732, 88
Guillot S., Servillat M., Webb N. A., Rutledge R. E., 2013, ApJ, 772, 7
Guillot S. et al., 2016, MNRAS, 463, 2612
Haensel P., Zdunik J. L., Schaefer R., 1986, A&A, 160, 121
Haggard D., Cool A. M., Anderson J., Edmonds P. D., Callanan P. J., Heinke C. O., Grindlay J. E., Bailyn C. D., 2004, ApJ, 613, 512
Harris W. E., 1996, AJ, 112, 1487
Harris W. E., 2010, preprint (arXiv:1012.3224)
Heinke C. O., Grindlay J. E., Lloyd D. A., Edmonds P. D., 2002, ASP Conf. Ser. Vol. 271, Variability and Spectra of Two Neutron Stars in 47 Tucanae, Astron. Soc. Pac., San Francisco. p. 349
Heinke C. O., Rybicki G. B., Narayan R., Grindlay J. E., 2006a, ApJ, 644, 1090
Heinke C. O., Wijnands R., Cohn H. N., Lugger P. M., Grindlay J. E., Pooley D., Lewin W. H. G., 2006b, ApJ, 651, 1098
Heinke C. O. et al., 2014, MNRAS, 444, 443
Hessels J. W. T., Ransom S. M., Stairs I. H., Freire P. C. C., Kaspi V. M., Camilo F., 2006, Science, 311, 1901
Ho W. C. G., Heinke C. O., 2009, Nature, 462, 71
Lattimer J. M., Prakash M., 2001, ApJ, 550, 426
Lattimer J. M., Prakash M., 2016, Phys. Rep., 621, 127
Lattimer J. M., Steiner A. W., 2014, ApJ, 784, 123
Lugger P. M., Cohn H. N., Heinke C. O., Grindlay J. E., Edmonds P. D., 2007, ApJ, 657, 286
Miller M. C., 2013, preprint (arXiv:1312.0029)
Miller M. C. et al., 2019, ApJ, 887, L24
Nandra K. et al., 2013, preprint (arXiv:1306.2307)
Nättilä J., Miller M. C., Steiner A. W., Kajava J. J. E., Suleimanov V. F., Poutanen J., 2017, A&A, 608, A31
O'Malley E. M., Gilligan C., Chaboyer B., 2017, ApJ, 838, 162
Oppenheimer J. R., Volkoff G. M., 1939, Phys. Rev., 55, 374
Özel F., Freire P., 2016, ARA&A, 54, 401
Pancino E., Bellazzini M., Giuffrida G., Marinoni S., 2017, MNRAS, 467, 412
Patruno A., Watts A. L., 2012, preprint (arXiv:1206.2727)
Pooley D., Homan J., Heinke C., Linares M., Altamirano D., Lewin W., 2010, Astron. Telegram, 2974, 1
Raaijmakers G. et al., 2019, ApJ, 887, L22
Raaijmakers G. et al., 2020, ApJ, 893, L21
Rajagopal M., Romani R. W., 1996, ApJ, 461, 327
Rawls M. L., Orosz J. A., McClintock J. E., Torres M. A. P., Bailyn C. D., Buxton M. M., 2011, ApJ, 730, 25
Ray P. S., Arzoumanian Z., Gendreau K. C., 2018, in Weltevrede P., Perera B. B. P., Preston L. L., Sanidas S., eds, Proc. IAU Symp. 337, Pulsar Astrophysics the Next Fifty Years. Kluwer, Dordrecht, p. 187
Riley T. E. et al., 2019, ApJ, 887, L21
Rivera Sandoval L. E. et al., 2018, MNRAS, 479, 2777
Rutledge R. E., Bildsten L., Brown E. F., Pavlov G. G., Zavlin V. E., 2002, ApJ, 577, 346
Rutledge R. E., Fox D. W., Kulkarni S. R., Jacoby B. A., Cognard I., Backer D. C., Murray S. S., 2004, ApJ, 613, 522

Sanna A. et al., 2017, A&A, 598, A34
Servillat M., Heinke C. O., Ho W. C. G., Grindlay J. E., Hong J., van den Berg M., Bogdanov S., 2012, MNRAS, 423, 1556
Srinivasan G., van den Heuvel E. P. J., 1982, A&A, 108, 143
Steiner A. W., Heinke C. O., Bogdanov S., Li C. K., Ho W. C. G., Bahramian A., Han S., 2018, MNRAS, 476, 421
Strohmayer T., Bildsten L., 2006, New views of thermonuclearbursts, Cambridge University Press, Cambridge, p. 113
Tauris T. M., van den Heuvel E. P. J., 2006, Formation and Evolution of Compact Stellar X-Ray Sources, Cambridge University Press, Cambridge. p. 623
Tolman R. C., 1939, Phys. Rev., 55, 364
Verbunt F., Lewin W. H. G., 2006, Globular Cluster X-ray Sources, Cambridge University Press, Cambridge, p. 341
Verner D. A., Ferland G. J., Korista K. T., Yakovlev D. G., 1996, ApJ, 465, 487
Walsh A. R., Cackett E. M., Bernardini F., 2015, MNRAS, 449, 1238
Watts A. L., 2019, AIP Conference Proc., 2127, 020008, preprint (arXiv: 1904.07012)
Webb N. A., Barret D., 2007, ApJ, 671, 727
Wijnands R., Degenaar N., Page D., 2017, J. Astrophys. Astron., 38, 49
Wilms J., Allen A., McCray R., 2000, ApJ, 542, 914
Zavlin V. E., Pavlov G. G., Shibanov Y. A., 1996, A&A, 315, 141
Zurek D. R., Knigge C., Maccarone T. J., Dieball A., Long K. S., 2009, ApJ, 699, 1113

APPENDIX A:

Table A1. Spectral fit parameters for `nsatmos` and `nsx`, for individual 2017 spectra. The statistical fits are χ^2_ν/dof (prob.) = 0.96/125 (0.62) for `nsatmos`, and χ^2_ν/dof (prob.) = 0.95/125 (0.63) for `nsx`. The values in parentheses correspond to fixed parameters in the models, while other values are obtained from the MCMC posterior medians. All reported uncertainties correspond to the 5 per cent and 95 per cent quantiles, i.e. representing the 90 per cent credible intervals.

Model parameter	Group 1 (2001)	Group 2 (2017)
	`nsatmos`	
Frame time (s)	(3.14)	(0.941)
$\alpha_{\rm pileup}$	$0.09^{+0.51}_{-0.09}$	$<0.78^a$
$N_{\rm H}$ (10^{20} cm^{-2})	$1.20^{+2.72}_{-1.09}$	
$kT_{\rm eff}$ (eV)	$106.46^{+29.97}_{-14.19}$	
$M_{\rm NS}$ ($M_\odot$)	$1.06^{+0.50}_{-0.51}$	
$R_{\rm NS}$ (km)	$8.63^{+2.75}_{-1.98}$	
Γ^b	(1.5)	
PL norm (10^{-15} erg s^{-1} cm^{-2})^a	<0.005	<0.008
	`nsx`	
Frame time (s)	(3.14)	(0.941)
$\alpha^{\rm a}_{\rm pileup}$	<0.001	$<2.72 \times 10^{-5}$
$N_{\rm H}$ (10^{20} cm^{-2})	$2.24^{+2.88}_{-1.90}$	
$kT_{\rm eff}$ (eV)	$94.35^{+20.24}_{-11.42}$	
$M_{\rm NS}$ ($M_\odot$)	$1.19^{+0.74}_{-0.60}$	
$R_{\rm NS}$ (km)	$11.30^{+3.59}_{-2.42}$	
Γ^b	(1.5)	
PL Norm (10^{-15} erg s^{-1} cm^{-2})^a	<0.006	<0.007

[a]Corresponds to the 90 per cent confidence upper limit.
[b]Represents the photon index of the power-law model.

Table A2. The best-fitting fluxes for individual 2017 observations estimated from the MCMC posterior medians, where uncertainties correspond to the 5 per cent and 95 per cent quantiles.

ObsID	$\log_{10}(F/\,{\rm erg\ cm^{-2}\ s^{-1}})$
18997	$-13.14^{+0.05}_{-0.05}$
20725	$-13.23^{+0.10}_{-0.12}$
20726	$-13.12^{+0.09}_{-0.12}$
20731	$-13.08^{+0.08}_{-0.10}$
20732	$-13.12^{+0.06}_{-0.06}$
20792	$-13.10^{+0.07}_{-0.08}$
20795	$-13.25^{+0.12}_{-0.16}$
20796	$-13.09^{+0.07}_{-0.08}$

This paper has been typeset from a TEX/LATEX file prepared by the author.